

# Diffraction efficiency of a small-period astronomical x-ray reflection grating fabricated using thermally activated selective topography equilibration

Ross C. McCurdy<sup>✉,\*</sup>, Drew M. Miles<sup>✉</sup>, Jake A. McCoy<sup>✉</sup>, Fabien Grisé<sup>✉</sup>,  
and Randall L. McEntaffer

The Pennsylvania State University, Department of Astronomy and Astrophysics,  
University Park, Pennsylvania, United States

**Abstract.** We have fabricated a blazed x-ray reflection grating with a period of 160 nm using thermally activated selective topography equilibration (TASTE) and electron-beam (ebeam) physical vapor evaporation. TASTE makes use of grayscale ebeam lithography to create three-dimensional (3-D) structures in resist, which can then be thermally reflowed into a desired profile. A blazed grating profile can be fabricated by selectively reflowing a periodic staircase structure into a wedge. This was done for the first time at a grating period of 160 nm, 2.5 times smaller than previous x-ray gratings fabricated using TASTE. The grating was patterned over a 10 mm by 60 mm area in a 147-nm-thick layer of poly(methyl methacrylate) resist and coated with 5 nm of chromium and 15 nm of gold using ebeam evaporation. The diffraction efficiency of the grating was measured using beamline 6.3.2 at Lawrence Berkeley National Laboratory's Advanced Light Source. The results show a total absolute diffraction efficiency  $\gtrsim 40\%$  at lower energies, with maximum single-order diffraction efficiency ranging from 20% to 40%. The total diffraction efficiency was  $\gtrsim 30\%$  across the measured bandpass of 180 to 1300 eV. © 2020 Society of Photo-Optical Instrumentation Engineers (SPIE) [DOI: [10.1117/1.JATIS.6.4.045003](https://doi.org/10.1117/1.JATIS.6.4.045003)]

**Keywords:** nanofabrication; instrumentation; astronomy; gratings; x-ray gratings.

Paper 20060 received May 29, 2020; accepted for publication Oct. 19, 2020; published online Nov. 5, 2020.

## 1 Introduction

As the needs of the astronomical community exceed the capabilities of current x-ray observatories, development of highly sensitive x-ray instrumentation is necessary to enable the goals of the next generation of x-ray missions. High-resolution soft-x-ray spectroscopy (0.2 to 2.0 keV) is required to address astrophysical questions about the formation and evolution of galaxies and large-scale structures.<sup>1-3</sup> Lynx, one of four large mission concepts currently being studied for the 2020 Decadal Survey, aims to address these questions.<sup>1,3</sup> One of Lynx's proposed observational campaigns is an x-ray-absorption-line study of the circumgalactic medium of galaxies with large halos ( $\gtrsim 10^{12} M_{\odot}$ ) using background active galactic nuclei. The survey aims to detect OVII and OVIII absorption lines in hot gas ( $\gtrsim 10^6$  K) down to equivalent widths of 1 mÅ across various sightlines, halo masses, and impact parameters.<sup>3</sup> To conduct this survey, Lynx needs a spectrometer with a spectral resolving power of  $\lambda/\Delta\lambda = 5000$  and effective area of 4000 cm<sup>2</sup> between 0.45 to 0.7 keV.<sup>3</sup> An x-ray grating spectrometer is currently the only instrument that can meet these requirements.

Radially grooved, blazed x-ray reflection gratings in the off-plane mount have the potential to meet Lynx requirements.<sup>4</sup> X-ray reflection gratings in the off-plane mount are oriented such that the grooves are nearly parallel with the incident x-rays, which will strike the grating at grazing incidence. In this geometry the grating equation is

$$\sin(\alpha) + \sin(\beta) = \frac{n\lambda}{d \sin(\gamma)}, \quad (1)$$

---

\*Address all correspondence to Ross C. McCurdy, [rmccurdy@psu.edu](mailto:rmccurdy@psu.edu)

where  $\alpha$  is the azimuthal angle of the incident x-ray,  $\beta$  is the azimuthal angle of the diffracted x-ray,  $n$  is the order number,  $\lambda$  is the wavelength,  $d$  is the groove spacing, and  $\gamma$  is the half-cone opening angle between the incident x-ray and the groove direction.<sup>5</sup> In principle, a blazed grating will preferentially diffract x-rays in a plane perpendicular to the triangular facet at an angle  $\beta = 2\delta - \alpha$ , where  $\delta$  is the blaze angle.<sup>6,7</sup> The blaze wavelength,  $\lambda_b$ , is given as

$$\lambda_b = \frac{d \sin(\gamma)}{n} [\sin(2\delta - \alpha) + \sin(\alpha)]. \quad (2)$$

The diffraction efficiency of a wavelength of scientific interest in a given order is maximized when the grating is in the Littrow configuration where  $\alpha = \beta = \delta$ . In this setup, Eq. (2) simplifies to

$$\lambda_{b,\text{Littrow}} = \frac{2d \sin(\gamma) \sin(\delta)}{n}. \quad (3)$$

Figure 1(a) shows the geometry of reflection gratings in the off-plane mount while Fig. 1(b) shows a set of reflection gratings aligned in the Littrow configuration. The radial profile can also be seen in Fig. 1(b) as the groove density changes along the groove direction to match the converging beam from the telescope. This enables high spectral resolution by reducing grating-induced aberrations from a converging beam diffracting off a linear groove profile.<sup>10</sup> Reflection gratings operated in the off-plane mount have several characteristics that make them a promising candidate for meeting the requirements of Lynx and other future x-ray observatories: they can obtain high spectral resolving power, achieve high diffraction efficiency in a given bandpass due to blazing, and the geometry allows for many gratings to be stacked to obtain the required effective area for observatories.

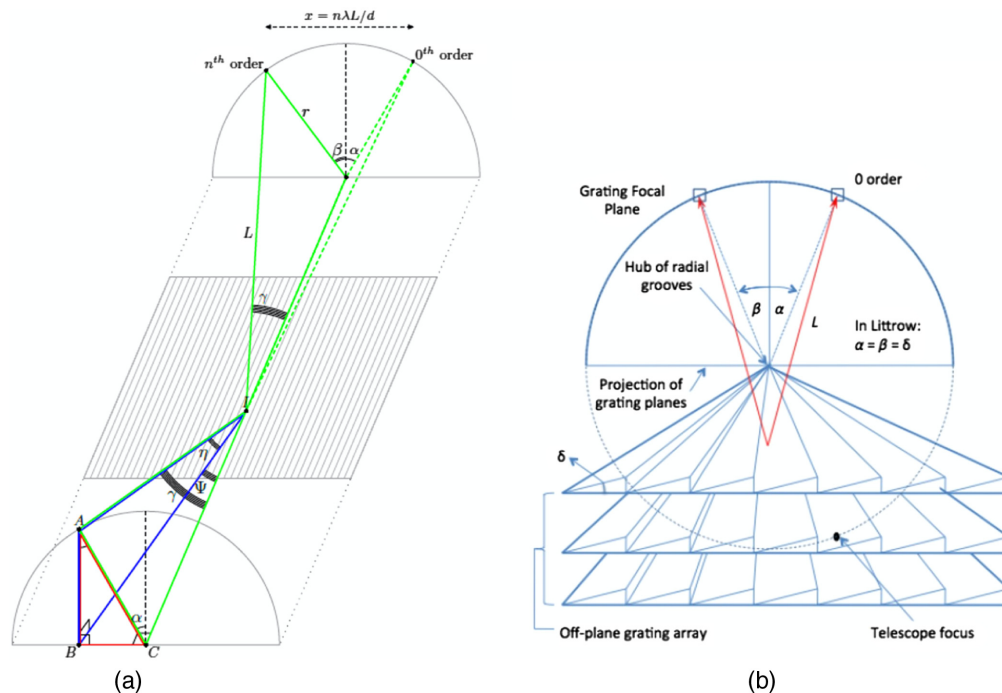


**Fig. 1** (a) Reflection-grating geometry in the off-plane mount.<sup>5</sup> A photon from point A with an azimuthal angle of  $\alpha$  and half-cone opening angle  $\gamma$  strikes the grating at position  $l$  with a graze angle of  $\eta$  and a yaw angle of  $\Psi$ . The photon either reflects to zero order or diffracts into an arc at a throw distance  $L$  away from  $l$  according to the generalized grating equation given in Eq. (1). Reproduced from Miles et al.<sup>8</sup> (b) Radially grooved reflection gratings in the Littrow configuration to maximize diffraction efficiency in a given bandpass. Incident x-rays are diffracted with high throughput into the blaze orders set by Eq. (3). Reproduced from McEntaffer et al.<sup>9</sup>

The current state-of-the-art methods for fabricating radial x-ray gratings make use of electron-beam lithography (EBL),<sup>7,8</sup> which is one of the few fabrication methods that can produce high-fidelity nanometer-size features with the control necessary for large-format radially grooved x-ray gratings. Electron-beam (ebeam) tools use a highly focused beam of electrons to expose a thin layer of polymeric resist coated on a substrate such as a silicon wafer. The electrons interact with the polymer leading to scission, reducing the molecular weight. This is known as a positive resist since the area exposed by the ebeam has a lower molecular weight.<sup>11</sup> After exposure, the resist is placed in a solvent (known as a developer) where the lower molecular weight polymers dissolve more quickly. After development, the pattern in the resist is transferred into the substrate or a hardmask such as silicon nitride using reactive ion etching. The resist is removed and the rectangular groove profile is anisotropically etched into the desired blaze profile. A common blazing technique for x-ray gratings is a potassium-hydroxide (KOH) wet etch.<sup>8,9,12-14</sup> The silicon substrate is submerged in KOH, which anisotropically etches down to the {111} crystal planes. Finally, the nitride hardmask is removed in a bath of hydrofluoric acid leaving a blazed profile.<sup>8,9,12-14</sup> X-ray reflection gratings that were blazed using KOH have been shown to achieve high diffraction efficiency. Measurements made using off-plane reflection gratings found the relative diffraction efficiency to be within 10% of the reflection limit of the gold coating and the absolute efficiency >60% across a significant portion of the tested bandpass.<sup>8</sup>

While KOH etching can produce high-efficiency gratings, the discrete spacing of the {111} crystal planes limits how accurately the pattern is transferred from the nitride hard mask to the silicon substrate during the KOH wet etch. For x-ray reflection gratings, the radial profile will snap to the nearest <111> plane with the spacing in the crystal plane exposed by the nitride hard mask given by  $s \simeq 0.3 \sin(\delta)$  nm, where  $\delta$  is the blaze angle set by the angle between the crystal plane exposed by the nitride mask and the <111> plane. The discretization of the radial profile places an upper limit on the resolving power of the grating spectrometer, which may be lower than mission (e.g., Lynx) requirements. There are two alternative methods being studied to fabricate blazed gratings: ion milling and thermally activated selective topography equilibration (TASTE). Ion milling is similar to reactive ion etching, but the angle between the ions and the substrate surface can be set by the user. A blazed grating is produced by first transferring the laminar ebeam pattern into the silicon substrate using reactive ion etching and then ion milling the grooves to create the desired asymmetrical groove profile.<sup>15,16</sup>

The blazing technique used in this study, TASTE, makes use of grayscale EBL to create multilevel structures in resist and thermally reflow them into a desired profile.<sup>6,7,17-20</sup> Grayscale EBL modulates the dose, the number of electrons per unit area, to create a lateral molecular-weight gradient in the resist. Next, there will be a gradient in the resist thickness with the thicker regions having been dosed less than the thinner regions and having a lower developer etch rate as a result of having a larger molecular weight.<sup>20</sup> After development, the resist is heated until it begins to flow, with lower molecular-weight regions flowing at lower temperatures. The resist flows both vertically and laterally, causing the grayscale profile to evolve in time. Various profiles can be achieved using combinations of reflow temperature, time, and grayscale pattern.<sup>20</sup> TASTE has previously been demonstrated to be able to create blazed groove profiles useful for x-ray gratings.<sup>6,7</sup> Gratings with custom groove profiles and patterns can be fabricated using TASTE that do not suffer from the same drawbacks as KOH etching. The groove pattern will not be discretized, and the blazed facets will follow the groove direction. These characteristics make TASTE a promising method to produce high-performance x-ray gratings that can meet the requirements of future observatories.

In this paper, we will present the results of the first diffraction-efficiency measurement of an x-ray grating fabricated using TASTE with a period of 160 nm,<sup>21</sup> 2.5 times smaller than what has previously been achieved with TASTE.<sup>6,7</sup> A smaller period increases the dispersion for a given grating setup and allows for greater flexibility in instrument design as well. While smaller periods are useful, they are difficult to fabricate and present new challenges compared to larger periods. In Sec. 2, we will discuss the fabrication of the grating. In Sec. 3, the test configuration and measurement results will be presented and will be discussed in Sec. 4. We present our conclusions in Sec. 5.

## 2 Grating Fabrication

In this section, each of the steps in the fabrication process for the tested grating will be discussed. All nanofabrication work was done at the Nanofabrication Lab in the Materials Research Institute at The Pennsylvania State University. Additional descriptions of the current TASTE fabrication process are given in McCoy et al.<sup>6,7</sup> The fabrication steps are similar to those in McCoy et al., while several (e.g. ebeam pattern/parameters, reflow conditions) have been adjusted for the new constant groove period of 160 nm.

A single-side polished, 100-mm-diameter silicon wafer was dynamically coated at 3000 rpm for 45 s with poly(methyl methacrylate) (PMMA) 950 A3, which is a 3% solution of PMMA in anisole with a molecular weight of 950 kg/mol. The sample was baked on a hotplate at 185°C for 3 min before and after spin coating to remove any residual moisture and to evaporate the anisole, respectively. The resist thickness was measured at seventeen points across the wafer using a J. A. WOOLLAM M-2000 focused ellipsometer to give an average measurement of  $147.30 \pm 0.04$  nm. The ebeam exposure pattern was prepared and fractured using BEAMER,<sup>22</sup> a software package developed by GeniSys that is used in pattern preparation for different lithographic processes. The pattern consists of three layers: a 40-nm-wide layer at 100% of the original resist thickness (unexposed), an 80-nm-wide layer at 60% resist thickness, and a 40-nm-wide layer at 0% resist thickness (cleared) to obtain a 160-nm period, and is shown in Fig. 2(a). The dose to achieve each of the thicknesses and account for the proximity effect was calculated using the 3DPEC module in BEAMER based on the contrast curve shown in Fig. 2(b). The pattern was arrayed to create a grating that was 10 mm in the cross-groove, or dispersion direction, and 60 mm in the groove direction. The sample was exposed using the RAITH EBPG5200 with a 40-nA beam and 400- $\mu$ m aperture, giving a beam spotsize of 34 nm. After exposure, the sample was developed using a bath of methyl isobutyl ketone (MIBK) and isopropyl alcohol (IPA) in a 1:1 ratio for 2 min, followed by a 30-s IPA rinse and nitrogen blow dry. No additional processing was done for 24 h after development to allow the resist swelling from development to dissipate. The sample was then heated at 108°C for 900 s using a vacuum hotplate to achieve uniform contact between the heating surface and the wafer.

The grayscale pattern and reflow conditions were determined by making a matrix of test samples using various patterns and reflow temperatures/times and measuring the profile using a BRUKER ICON atomic-force microscope (AFM). A viable pattern was chosen from that matrix and used for this grating. The sample was coated with a 5-nm adhesion layer of chromium and a 15-nm layer of gold for x-ray reflectivity using a TEMESCAL FC2000 ebeam evaporator. AFM data of the grating after each of these steps can be seen in Fig. 3. The final grating has an rms surface roughness ( $S_q$ ) of  $\sim 0.8$  nm with a range between 0.5 to 1.3 nm as measured with the AFM over

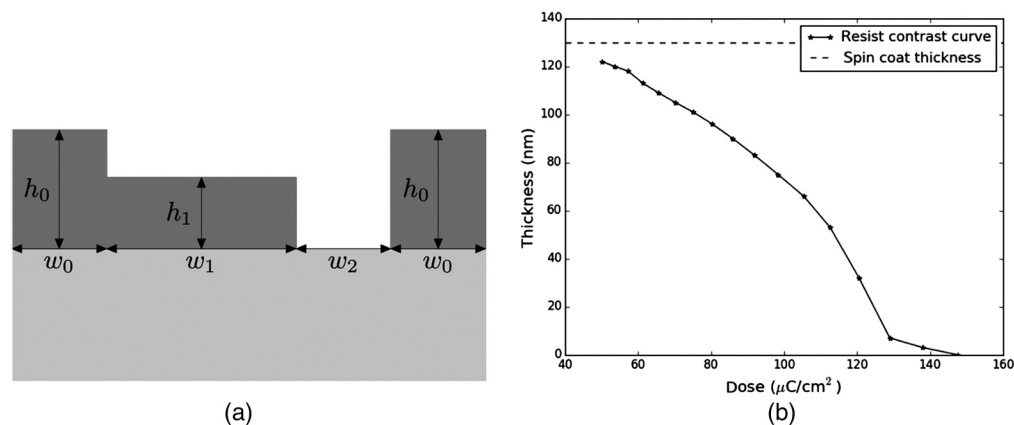


**Fig. 2** (a) Grayscale profile used in grating fabrication. The unexposed region has a thickness  $h_0$ , and is  $w_0 = 40$  nm wide. The first exposed region has a thickness of  $h_1 = 0.6 h_0$  and a width of  $w_1 = 80$  nm. The cleared region has a width of  $w_2 = 40$  nm. The sum of the widths of the three regions,  $d = w_0 + w_1 + w_2 = 160$  nm, is the period of the grating. (b) Contrast curve measured in McCoy et al.<sup>6</sup> The resist thickness is shown as a function of ebeam dose for a 130-nm-thick layer of PMMA developed at room temperature using 1:1 MIBK/IPA for 2 min and IPA for 30 s.

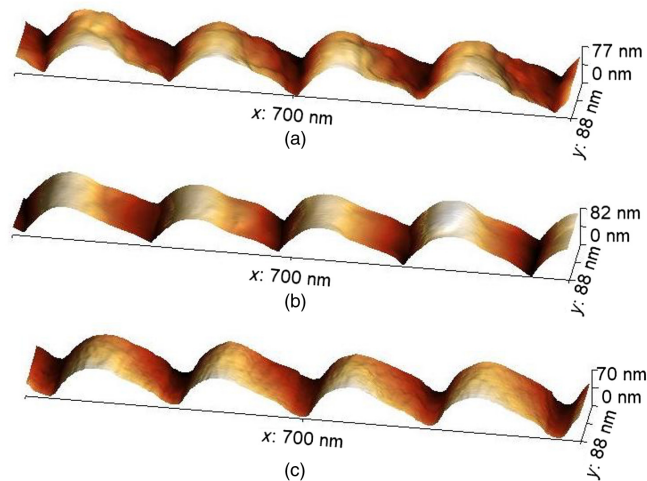


**Fig. 3** AFM images of the grating at different points in the fabrication process taken using a Bruker Icon AFM over 700 nm with 512 samples per line to give a 1.37-nm pixel size. (a) After grayscale exposure and development. (b) After reflow at 108°C for 900 s. (c) After deposition of 5 nm of chromium and 15 nm of gold.

50-nm square regions on the groove facets. The blaze angle is  $\sim 35$  degrees with a range between 28 and 39 degrees. The range was estimated by measuring blaze angles at various facet start/end points and different locations on the grating. It is difficult to obtain a precise measurement of the surface roughness and blaze angle from AFM data because the calculated values depend on what portion of the facet is used in the measurement. The rounding in the profile that can be seen in Fig. 3 makes it challenging to define where the blaze facet begins and ends, leading to a distribution of measurements. Pattern inhomogeneity resulting from the small feature sizes also contributes to the distribution.

### 3 Diffraction Efficiency

In this section, we will describe the diffraction-efficiency measurement performed using beamline 6.3.2 at Lawrence Berkeley National Laboratory's Advanced Light Source (ALS). The experimental setup and testing procedure is similar to the one discussed in the appendix of Miles et al.<sup>8</sup> A description of the test procedure will be given here.

#### 3.1 Grating Alignment

The grating was mounted onto stages that have six degrees of freedom: linear translations in  $x$ ,  $y$ , and  $z$ ; and rotation translations in pitch, yaw, and roll. The stage coordinate system can be seen in Fig. 4(a). The vacuum chamber has an external and internal CCD used for grating alignment and a photodiode for measuring the intensity of the x-ray beam. The first alignment step is to center the x-ray beam on the grating by imaging an optical beam that is coincident with the x-ray beam using the external CCD. Next, the grating is set to approximately zero pitch and moved in the  $z$  direction to occult half of the optical beam on the internal CCD. The grating pitch and  $z$  height are adjusted until the beam is occulted when the grating is negatively pitched and reflected when positively pitched. The internal CCD and photodiode are on an angular stage that travels in the pitch direction; the CCD is aligned with the x-ray beam when the stage is at zero degrees. The grating pitch (i.e., graze) is defined to be at  $\eta = 0$  deg when the grating is pitched an amount  $\Delta\eta > 0$  deg and the reflected beam spot is at an angle of  $2\Delta\eta$  on the angular stage. This is verified with the internal CCD using both the optical and x-ray beams. Once  $\eta = 0$  deg has been found, the grating is pitched to a grazing incidence angle; in this experiment, the graze angle was set to a nominal value of  $\eta = 1.5$  deg. The graze can be experimentally measured using the photodiode. A  $0.5 \times 10$  mm slit was mounted on the photodiode to isolate individual

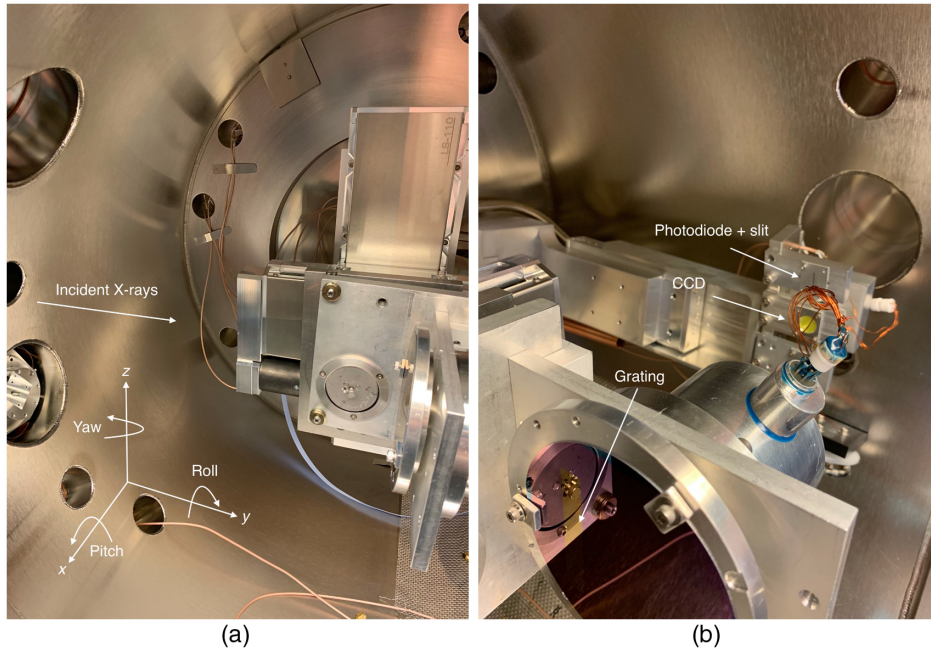


**Fig. 4** Beamline 6.3.2 vacuum chamber. (a) The grating mounted to the motorized stage with the coordinate system of the setup. It is worth noting that in this image, the grating is pitched 90 deg relative to the x-ray beam. (b) The photodiode covered with a  $0.5 \times 10 \text{ mm}^2$  slit, and the internal CCD. The grating pattern is offset from the center of the silicon wafer and marked with an arrow.

grating orders and can be seen in Fig. 4(b). The photodiode was scanned in the  $x$  direction (grating dispersion direction) to determine the position of zeroth order in the dispersion direction. Once found, the slit was scanned in the  $z$  direction (grating cross-dispersion direction) to identify the angular position of the centroid, which will be  $2\eta$ . This measurement was made twice at five energies and the mean graze angle was found to be  $\eta = 1.47 \pm 0.01$  deg. These data can also be used to measure the throw by using the measured cross-dispersion angular extent of zeroth order and the known physical size of the slit. The mean throw value was calculated to be  $L = 239 \pm 3$  mm. The roll can be calculated by measuring the change in the  $x$  position of diffraction orders as a function of graze angle. Data were collected at five graze angles and the mean roll was calculated to be  $\theta_{\text{roll}} = 1.2 \pm 0.4$  deg.

The final alignment step is to measure and adjust the yaw of the grating. In principle, the diffraction efficiency in a given bandpass is maximized in the Littrow configuration. For a given blaze angle,  $\delta$ , and graze angle,  $\eta$ , the yaw angle,  $\Psi$ , necessary to be in Littrow, can be determined using Eqs. (4) and (5),<sup>8</sup>

$$\cos(\alpha) = \cos(\delta)(\text{In Littrow}) = \frac{\sin(\eta)}{\sin(\gamma)}, \quad (4)$$

$$\cos(\Psi) = \frac{\cos(\gamma)}{\cos(\eta)}. \quad (5)$$

A blaze angle of  $\delta \approx 35$  deg with  $\eta = 1.47$  deg corresponds to a yaw of  $\Psi_{\text{Littrow}} = 1.03$  deg. The yaw is measured by performing a scan with the photodiode in the dispersion direction to determine the  $x$  centroids of the orders, and then finding the  $z$  centroids of each order in the cross-dispersion direction. The angular positions of the cross-dispersion centroids can be converted into physical distances using the throw of the system. This measurement is repeated at several energies to sample and then fit the diffraction arc. The yaw is related to the separation in the  $x$  direction between the zeroth-order centroid position,  $x_{\text{zero}}$ , and the hub of the arc,  $x_{\text{arc}}$ , the roll, the graze, and the throw

**Table 1** Grating geometry for the diffraction-efficiency measurement. Listed uncertainties are equal to  $1\sigma$ .

Graze ( $\eta$ ) (deg)	Yaw ( $\Psi$ ) (deg)	Roll ( $\theta_{\text{roll}}$ ) (deg)	Throw ( $L$ ) (mm)	$\gamma$ (deg)	$\alpha$ (deg)
$1.47 \pm 0.01$	$1.08 \pm 0.01$	$1.2 \pm 0.4$	$239 \pm 3$	$1.82 \pm 0.03$	$36.3 \pm 1.4$

$$\sin(\Psi) = \frac{x_{\text{zero}} - x_{\text{arc}}}{L \cos(\eta) \cos(\theta_{\text{roll}})}. \quad (6)$$

The yaw was calculated using Eq. (6) and adjusted until the grating was close to the Littrow configuration at  $\Psi = 1.08 \pm 0.01$  deg. The arc-of-diffraction radius,  $r$ , and throw are used to determine the half-cone opening angle,  $\gamma$ , given by Eq. (7)

$$\sin(\gamma) = \frac{r}{L}. \quad (7)$$

The value for  $\gamma$  can be substituted into Eq. (4) to calculate  $\alpha$  for the test geometry. Table 1 lists the values for the grating geometry used in this measurement.

The errors on the grating-geometry parameters were calculated using a Monte Carlo approach. Data sets were generated by taking the errors on the individual data points that consist of stage uncertainty and the photodiode measurement uncertainty,<sup>23</sup> and drawing new points from normal distributions centered about the data. The new data set is then passed through the relevant fitting routines and calculations to determine the grating geometry. Repeating this process several thousand times generated distributions for each of the grating angles, all of which except roll were verified to be normal using quantile-quantile plots. The listed uncertainties are the standard deviation of the distributions. While the roll is non-Gaussian, the standard deviation of 0.4 deg includes 62% of the distribution, which is close to the 65% within one standard deviation of a normal distribution, so it represents the width of the distribution well.

### 3.2 Diffraction-Efficiency Measurement

Diffraction-efficiency data were taken in 20-eV increments from 180 to 1300 eV. The photodiode was scanned in the  $x$  direction (dispersion direction) to capture all of the diffraction orders at each energy. The grating was also moved out of the beam so the direct-beam intensity could be measured. Several dark-current measurements were made for both the direct-beam and diffraction-order scans with the average values at each position subtracted out of the data. Peaks were identified in the data and the  $x$  positions of the diffraction orders were determined using a weighted mean with the intensities as the weights. The relative intensity at the centroid was calculated by taking the mean of the relative intensities of the two closest points about the centroid. The absolute diffraction efficiency is then given by the ratio of the relative intensities of the diffracted order and direct beam at their respective centroids. Uncertainties in the absolute efficiency were calculated by propagating photodiode measurement uncertainties through the centroid, mean, and ratio calculations. The efficiency uncertainty is quite small with values  $\lesssim 0.25\%$ . An example diffraction-order and direct-beam scan is shown in Fig. 5. The absolute diffraction efficiency as a function of energy is shown in Fig. 6. The relative diffraction efficiency, the ratio of absolute diffraction efficiency to the gold-coating reflectivity, is shown in Fig. 7. The gold-coating reflectivity shown in Fig. 6 was used to calculate the relative diffraction efficiency for this test geometry and obtained from the Center for X-ray Optics' (CXRO) X-ray Database.<sup>24</sup> Relative diffraction efficiency gives an understanding of grating performance independent of the reflective coating used. Uncertainties are included in Figs. 6 and 7 but are smaller than the plot points.

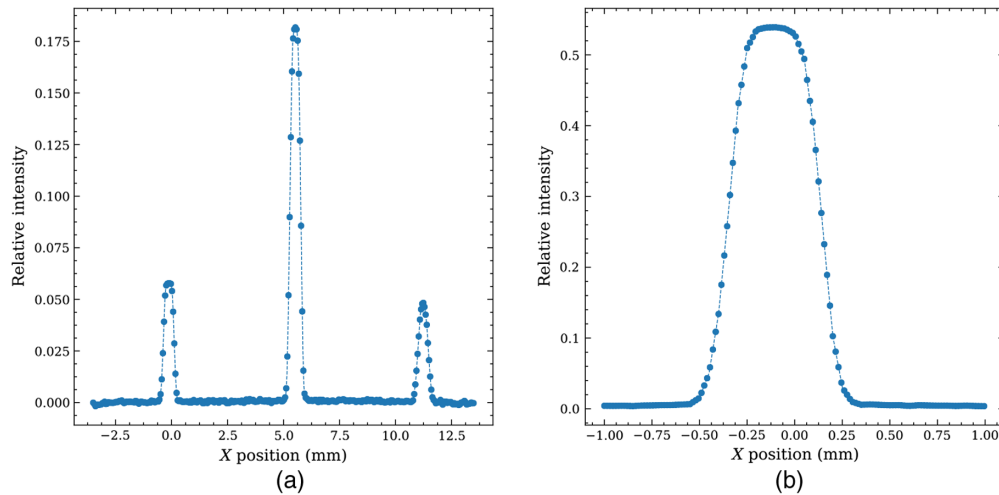


**Fig. 5** Diffraction-efficiency measurement scans at 340 eV. (a) Diffraction-order scan, orders from left to right are: zeroth, first, and second. (b) Direct-beam scan.

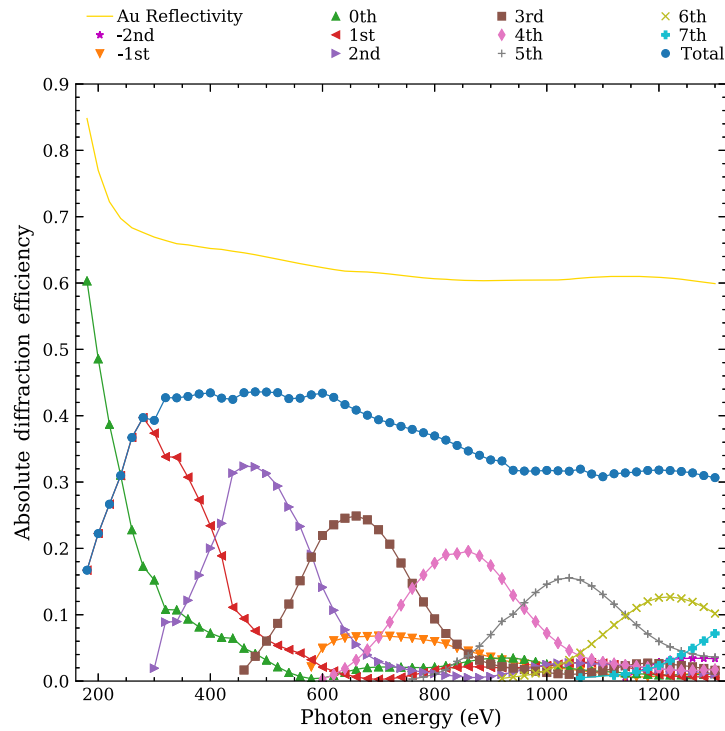


**Fig. 6** Absolute diffraction efficiency as a function of energy. The total diffraction efficiency is the sum of all the orders shown excluding zeroth order. The Au reflectivity for an incidence angle of 1.82 degrees with a 0.8-nm rms surface roughness was obtained from the CXRO X-ray Database and is shown as a solid gold line in the figure.

## 4 Discussion

The grating achieved a total diffraction efficiency above 40% for energies below  $\sim 670$  eV, with the majority of the efficiency coming from a single or a few orders, typically first through third order. The Lynx effective area requirement of  $4,000 \text{ cm}^2$  between  $0.45\text{--}0.7 \text{ keV}^3$  corresponds to an absolute grating efficiency of 40% at OVII.<sup>4</sup> The diffraction efficiency at 580 eV, close to the OVII energy of 574 eV, is 43% with 2% coming from negative first order, 3% from first order,

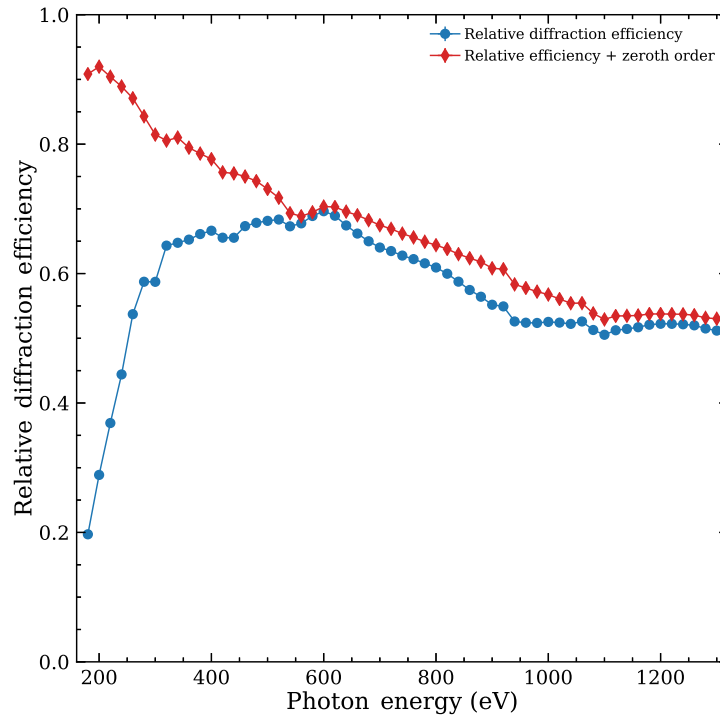


**Fig. 7** Relative diffraction efficiency as a function of photon energy. The blue data are the absolute diffraction efficiency as a fraction of the gold reflectivity excluding zeroth order. The red data are the relative efficiency including zeroth order.

19% from second order, and 18% from third order. Single-order diffraction efficiencies are highest at lower energies, reaching peaks of 40%, 33%, and 25% for first, second, and third order, respectively. The total absolute efficiency begins to decrease at higher energies, leveling off at 30% around 900 eV. The diffracted x-rays are also spread out between multiple orders, with peak single-order efficiencies below 20% starting at fourth order. The single-order and total diffraction efficiency of this grating are lower than what a 400-nm period TASTE grating tested in a similar configuration at ALS achieved over their shared bandpass of 180 to 800 eV.<sup>7</sup> This is due to a fraction of the flux incident on the grating being lost from a combination of processes, likely different forms of scattering. This can be seen in Fig. 7, where the relative diffraction efficiency including zeroth order starts at  $\sim 0.9$  at 180 eV and decreases across the entire measured bandpass to  $\sim 0.5$  at 1300 eV. In an ideal grating, this value should be close to one with some losses expected from surface roughness. Gratings previously tested at ALS, such as the 400-nm TASTE grating and a replicated 160-nm KOH grating, have relative efficiencies including zeroth order  $\gtrsim 0.9$  across their measured bandpass.<sup>7,8</sup>

There are two forms of scattering of interest in understanding grating performance: scattering into the medium (absorption), and diffraction from roughness features leading to diffuse scatter out of the medium (vacuum scattering). The medium is the 15-nm layer of gold deposited onto the TASTE profile via ebeam evaporation. The roughness profile of the gold layer is a combination of roughness present in the TASTE profile due to the lithographic and thermal reflow processes, as well as roughness from the deposition process. To understand the scattering effects resulting from roughness, the incidence angle of the photon striking the groove facet,  $\zeta$ , must be considered. The term  $\zeta$  is related to  $\alpha$ ,  $\gamma$ , and  $\delta$  by

$$\sin(\zeta) = \sin(\gamma) \cos(\delta - \alpha), \quad (8)$$

and is shown geometrically in Fig. 8.<sup>6,7</sup> It is worth noting that in the Littrow configuration  $\zeta = \gamma$ . Inserting values from Table 1 into Eq. (8) and taking the blaze angle found from modeling the efficiency data,  $\delta = 38$  deg,  $\zeta \simeq 1.82$  deg  $\simeq \gamma$  as expected for the near-Littrow configuration the grating was tested in. The attenuation length of gold in the direction normal to the groove

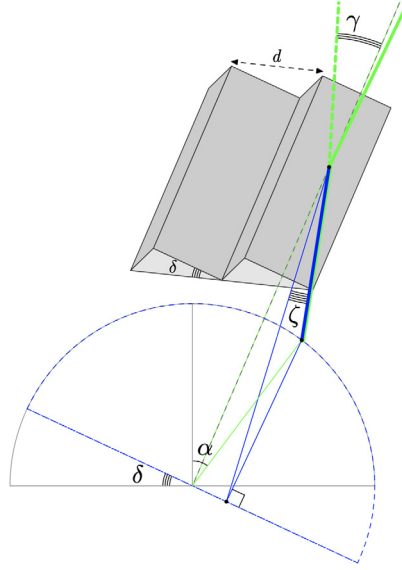


**Fig. 8** The incidence angle,  $\zeta$ , of a photon striking the groove facet. The incidence angle is related to  $\alpha$ ,  $\gamma$ , and  $\delta$  by  $\sin(\zeta) = \sin(\gamma) \cos(\delta - \alpha)$ .<sup>6,7</sup>

facet,  $l_{\text{Au}}$ , at an incidence angle of  $\zeta = 1.82$  deg obtained from the CXRO database is  $1.66 \text{ nm} \lesssim l_{\text{Au}} \lesssim 3.12 \text{ nm}$  in the 180- to 1300-eV bandpass. The surface layer of gold can then be described as a thick slab since an x-ray reflecting off the gold-chromium interface would need to travel a distance  $\gtrsim 10 l_{\text{Au}}$ , which has a very low probability of occurring ( $\lesssim e^{-10}$ ). The effects of surface roughness on the specular reflectivity of a thick slab can be approximated using the Nevot–Croce factor (NCF);<sup>25,26</sup> its application to reflection gratings in the off-plane mount is addressed in McCoy et al.<sup>7</sup> The NCF is defined as the ratio of the reflectivity of a rough surface,  $\mathcal{R}_{\text{rough}}$ , and the Fresnel reflectivity,  $\mathcal{R}_F$ ,

$$\text{NCF} = \frac{\mathcal{R}_{\text{rough}}}{\mathcal{R}_F} = \left\| \exp(-2k_{\perp} \tilde{k}_{\perp} \sigma^2) \right\|^2 = \exp\left(-4\sigma^2 k_0^2 \sin(\zeta) \text{Re}\left[\sqrt{\tilde{\nu} - \cos^2(\zeta)}\right]\right), \quad (9)$$

where  $k_{\perp} = k_0 \sin(\zeta)$ ,  $\tilde{k}_{\perp} = k_0 \sqrt{\tilde{\nu} - \cos^2(\zeta)}$ ,  $k_0 = 2\pi/\lambda$  is the photon wavenumber,  $\tilde{\nu}$  is the complex index of refraction of the material,  $\sigma$  is the rms surface roughness, and the Fresnel reflectivity is given by

$$\mathcal{R}_F = \left\| \frac{\sin(\zeta) - \sqrt{\tilde{\nu} - \cos^2(\zeta)}}{\sin(\zeta) + \sqrt{\tilde{\nu} + \cos^2(\zeta)}} \right\|^2. \quad (10)$$

Equation (10) describes the Fresnel reflectivity for a wavefront with transverse-electric polarization, which, at grazing incidence in the soft-x-ray regime, is approximately equal to the transverse-magnetic polarization.<sup>7,27</sup> The NCF assumes normally distributed, small roughness features satisfying the condition  $k_{\perp} \sigma \ll 1$ .<sup>7,26</sup> Rewriting this in terms of photon energy and substituting in  $\zeta = 1.82$  deg and the typical rms surface roughness obtained with AFM measurements,  $\sigma \approx 0.8 \text{ nm}$ ,

$$E_{\text{photon}} = \frac{hc}{\lambda} \ll \frac{1240 \text{ eV} \cdot \text{nm}}{2\pi\sigma \sin(\zeta)} \approx 7770 \text{ eV}. \quad (11)$$

Furthermore, the NCF has a surface correlation length,  $\xi$ , included in the derivation that satisfies the condition  $\xi k_{\perp}^2 \ll k_0$ .<sup>7,25,26</sup> This term can also be rewritten in terms of photon energy,

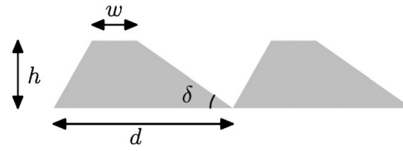


**Fig. 9** Trapezoidal groove profile used in the PCGrate-SX grating diffraction-efficiency models. The trapezoid was given similar characteristics to the measured grating values, with a height of  $h = 65$  nm, top width of  $w = 10$  nm, period of  $d = 160$  nm, and blaze angle of  $\delta = 38$  deg.

$$E_{\text{photon}} = \frac{hc}{\lambda} \ll \frac{1240 \text{ eV} \cdot \text{nm}}{2\pi\xi \sin^2(\zeta)} \approx 1960 \left( \frac{100 \text{ nm}}{\xi} \right) \text{ eV}. \quad (12)$$

If the conditions in Eqs. (11) and (12) are met, then diffuse scatter resulting from diffraction off the roughness features can be neglected and only absorption need be considered.<sup>7,26</sup> PCGrate-SX, the software package used for modeling the grating performance discussed below, models losses due to surface roughness under the assumption that both of these conditions are met.

The theoretical grating performance was modeled using the PCGrate-SX software package. PCGrate solves the Helmholtz equation to calculate the diffraction efficiency of a grating setup specified by the user.<sup>28,29</sup> A grating was set up in PCGrate using the geometry listed in Table 1. The PCGrate model uses a trapezoidal groove profile with the nominal period, depth, and blaze angle as the TASTE profile and is shown in Fig. 9. A flat top was used instead of a rounded profile because PCGrate has trouble modeling rounded profiles that do not fit certain functional forms. A blaze angle of  $\delta = 38$  deg was used in the models to qualitatively match the blaze peaks in the model to the data. While the model blaze angle is different from the nominal value of  $\delta \approx 35$  deg, it is within the range of angles measured with the AFM discussed in Sec. 2. Changing the blaze angle from  $\delta = 38$  deg shifts the model peaks to higher or lower energies for smaller and larger angles, respectively. A 15-nm layer of gold was added to the grating with the surface roughness set to match the measured AFM value of 0.8-nm rms. The index of refraction in the model comes from the CXRO database mentioned previously. A plot of the model and measured data is shown in Fig. 10. The PCGrate model shown in Fig. 10 does a decent job of reproducing some trends in the measured data, specifically the shape of the orders and the general locations of the blaze peaks. The peak efficiencies of the diffraction orders and the total diffraction efficiency are greater than the data, especially at higher orders where the model efficiency decreases more gradually than the data. Another model is shown in Fig. 11 where the surface roughness has been increased from the AFM value of  $\sim 0.8$  to 3.25 nm rms. This model does a better job of reproducing the behavior in the data, especially for zero-third order and the total efficiency.

While the second model fits the data better, the increased roughness falls well outside the range of measured roughness values (0.5 to 1.3 nm rms). Figure 12 shows the NCF and the difference between the NCF and the relative diffraction efficiency including zeroth order. The NCF was calculated for the gold layer using Eq. (9) with  $\zeta = 1.82$  deg, an rms surface roughness of 0.8 nm, and the complex index of refraction of gold from the CXRO database. If the NCF accurately describes the efficiency losses due to surface roughness, it will be very close to the relative diffraction efficiency including zeroth order. The calculated difference ranges from  $\sim 0.1$  to 0.45 across the bandpass. Combined with the results in Fig. 12, the need to greatly increase the surface roughness from the measured range suggests that diffuse vacuum scatter cannot be ignored, and at least one of the conditions given by Eqs. (11) and (12) for the Nevot-Croce approximation is not being met. It is likely that the condition in Eq. (11) is satisfied, as the highest energy in the tested bandpass, 1300 eV, is a factor of 6 lower than the limiting photon energy,  $E_{\text{photon}} \ll 7770$  eV. This decreases to a factor of 3.6 when the roughness is on the upper end of the measured values at 1.3 nm rms. Even in this case, the majority of the bandpass from 180 to 1300 eV comfortably satisfies this condition. It is more likely then, that the second condition relating to the correlation length given in Eq. (12) is not satisfied. While the true profile of the grating surface roughness (typically characterized by a power spectrum) and

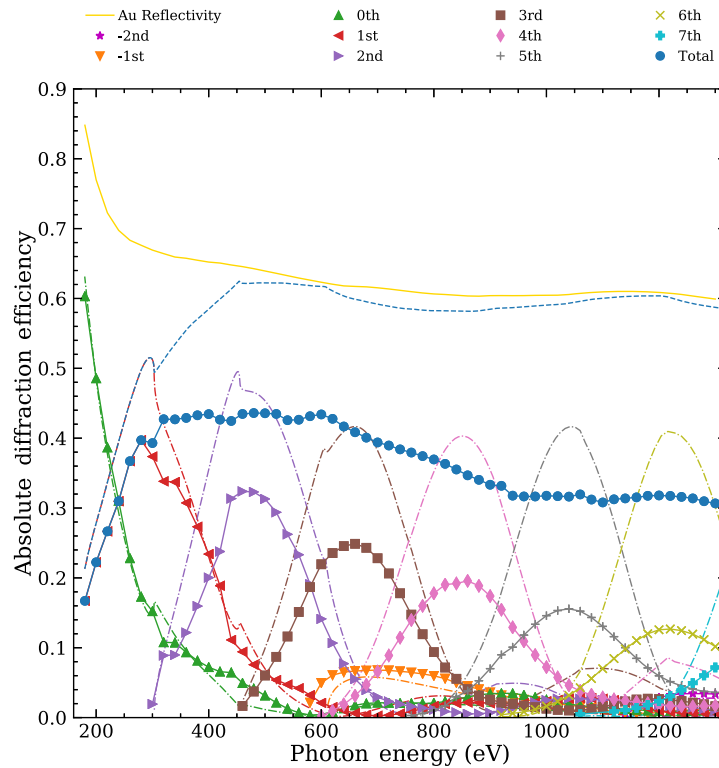


**Fig. 10** Theoretical and measured diffraction efficiency as a function of energy. The data are shown as points with connecting lines, while the modeled efficiency from PCGrate is shown as dot-dash lines for the diffraction orders with each modeled order being centered above the corresponding measured order data. The total model efficiency excluding zeroth order is shown as a dashed line. The Au reflectivity is shown as a solid gold line.

its correlation length,  $\xi$ , are unknown, if  $\xi \simeq 100$  nm then Eq. (12) requires  $E_{\text{photon}} \ll 1960$  eV, which is not necessarily true for the tested bandpass. Larger values of  $\xi$  would exacerbate this and increase the amount of diffuse vacuum scatter. The large amount of diffuse scatter inferred from the difference between the NCF and the relative diffraction efficiency in Fig. 12 suggests a correlation length that does not satisfy Eq. (12). There is additional evidence for scattering present in the cross-dispersion scans taken at multiple energies during grating alignment. Future ALS measurements will need to include scans to better understand the amount and location of the scatter as a function of photon energy.

In addition to efficiency losses due to surface roughness, the intensity of the diffracted orders is also modified as a result of line-edge roughness (LER) and line-width roughness (LWR) present in the grating. LER is the change of the center position of the groove while the groove width is constant, whereas LWR describes the change of the groove width while the center is kept constant.<sup>30,31</sup> The effects of LER and LWR on the diffraction orders of lamellar gratings at grazing incidence have been derived analytically following the derivation of the Debye–Waller factor (DWF).<sup>30,32,33</sup> The intensity of a diffracted order due to mutually independent LER and LWR is modified as

$$\text{DWF} = \frac{I(k)}{I_0(k)} = \exp(-\Sigma^2 k^2), \quad (13)$$

where  $k$  is the wavenumber of the order,  $I_0$  is the Fraunhofer diffraction intensity of a grating with  $N$  slits normalized to the specular reflected intensity  $I(k=0)$ ,  $\Sigma^2 = \sigma_{\text{LER}}^2 + \frac{1}{4}\sigma_{\text{LWR}}^2$ ,  $\sigma_{\text{LER}}$  is the variance of the LER distribution, and  $\sigma_{\text{LWR}}$  is the variance of the LWR distribution.<sup>30</sup> The DWF was added to the PCGrate diffraction efficiency models to determine whether the combined Debye-Waller and Nevot-Croce factors could better describe the measured diffraction

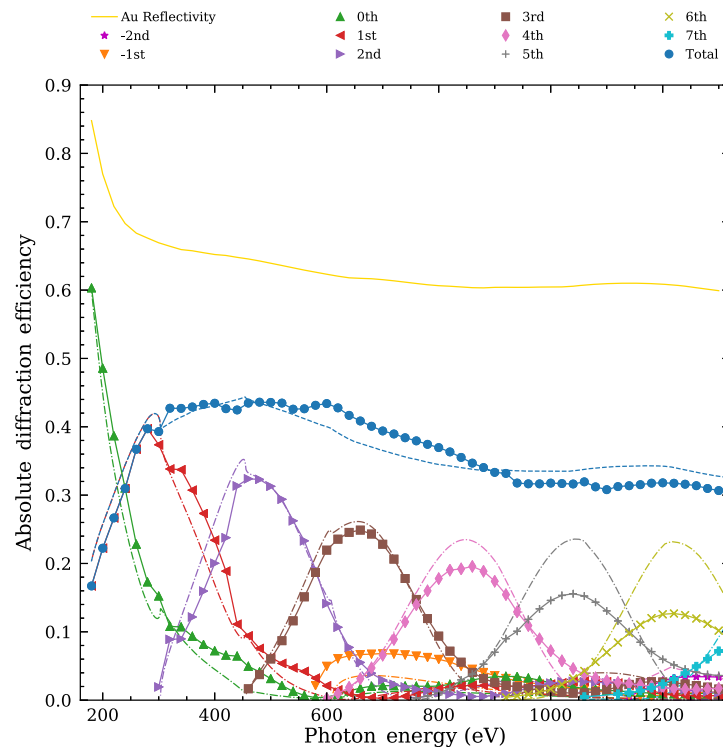


**Fig. 11** Theoretical and measured diffraction efficiency as a function of photon energy. The theoretical model has an increased surface roughness of 3.25-nm rms. The data are shown as points with connecting lines, while the modeled efficiency from PCGrate is shown as dot-dash lines for the diffraction orders with each modeled order being centered above the corresponding measured order data. The total model efficiency excluding zeroth order is shown as a dashed line. The Au reflectivity for 0.8-nm rms surface roughness is shown as a solid gold line.

efficiency of the grating. The PCGrate models were modified to include the DWF by multiplying the modeled diffraction efficiency of every energy in a given order by the exponential term in Eq. (13). The wavenumber for each diffraction order is given by  $k = 2\pi n/d$ , where  $n$  is the order number and  $d$  is the nominal groove period of 160 nm.<sup>30</sup> The LER/LWR variance term,  $\Sigma$ , was adjusted to qualitatively match the modeled and measured total diffraction efficiency. Figure 13 shows the modeled diffraction efficiency with the nominal measured surface roughness of 0.8-nm rms and  $\Sigma = 3.5$  nm. This model does a better job of capturing the decrease in total and single-order efficiency as energy increases compared to the model shown in Fig. 10, which only uses the NCF. Figure 14 shows a model with the rms surface roughness set to 2.8 nm and  $\Sigma = 2.35$  nm. These parameters also do a better job of qualitatively reproducing the total diffraction efficiency compared to the NCF-only model shown in Fig. 11 with a 3.25-nm rms roughness. Including the DWF reduces the necessary NCF rms surface roughness while providing a moderately better fit, however, the NCF surface roughness still falls outside of the measured range.

While the combination of the Nevot–Croce and Debye–Waller factors offers a better description of the measured total diffraction efficiency, notable differences between the modeled and measured single-order diffraction efficiency peaks and profiles are still present. This is likely a result of several factors. The groove profile used in the PCGrate simulations, shown in Fig. 9, is an approximation to the measured profile shown in Fig. 3. Different groove profiles will redistribute power in the blaze orders, even if the total diffraction efficiency is similar. This effect can be seen in the figures comparing modeled and measured data, where measured orders often have broader or narrower profiles and lower peak efficiency values than modeled orders. There is a distribution of groove profiles present in the TASTE grating as well that also contributes to the profile of the measured blaze orders. Additionally, both the NCF and DWF have conditions that need to be satisfied to accurately model the effects of roughness on the diffraction efficiency.

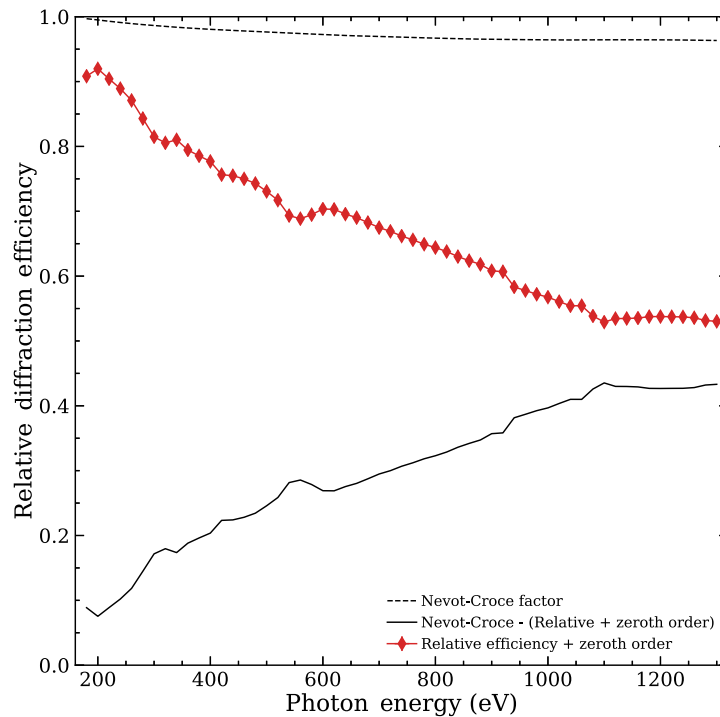


**Fig. 12** The NCF and relative diffraction efficiency as a function of photon energy. The red data are the relative efficiency including zeroth order. The dashed black line is the NCF for a gold layer with an rms surface roughness of 0.8 nm calculated using Eq. (9) and the index of refraction from the CXRO database. The solid black line is the difference between the NCF and the relative diffraction efficiency including zeroth order.

The NCF conditions are given by Eqs. (11) and (12); the increase in the rms surface roughness value above the measured AFM range suggests Eq. (12) is not met as discussed previously. The DWF derivation of Eq. (13) assumes a laminar grating and that: the LER and LWR distributions are the same for all grooves; the displacement,  $\Delta_{\text{LER}}$ , of the groove position from its ideal location due to LER is small and centered about 0; the value of  $\Delta_{\text{LWR}}$ , the change in the groove width from its nominal value, is small and centered about 0; and that both  $\Delta_{\text{LER}}$  and  $\Delta_{\text{LWR}}$  are normally distributed about 0 with a variance of  $\sigma_{\text{LER}}^2$  and  $\sigma_{\text{LWR}}^2$ , respectively.<sup>30</sup> The TASTE grating is blazed rather than laminar, and the wedge shape of the groove profile makes it unclear how to define LER and LWR as there are not obvious edges on the grooves. As such, it is difficult to measure the LER and LWR to verify that the corresponding  $\Delta$  is small and normally distributed about 0. The roughness distribution parameter,  $\Sigma$ , was adjusted without changing  $\sigma_{\text{LER}}$  or  $\sigma_{\text{LWR}}$  individually because they are neither clearly defined nor measured for the TASTE grating. The reported values of  $\Sigma$  are not necessarily physically representative of the true grating and should not be interpreted as such. While all of the conditions on the DWF given by Eq. (13) are not met by the TASTE grating, the DWF does a better job of qualitatively modeling the diffraction efficiency when combined with the NCF compared to the NCF alone. This suggests a more complex model accurately incorporating effects from both the surface roughness and LER/LWR of a blazed grating is necessary to better describe the diffraction efficiency data. An improved groove profile that is more representative of the true profile would also benefit the modeling.

As mentioned previously, the 400-nm TASTE grating tested at ALS has a greater relative efficiency including zeroth order than the 160-nm grating tested here with  $\gtrsim 0.9$  across their shared 180- to 800-eV bandpass. Additionally, the NCF accurately models the efficiency loss of the 400-nm grating due to surface roughness,<sup>7</sup> whereas the 160-nm TASTE grating has additional scattering at higher orders. There is no indication of a significant amount of diffuse vacuum scattering occurring in the 400-nm grating, suggesting that the two TASTE gratings have very different roughness profiles. The difference in the roughness profile between the two

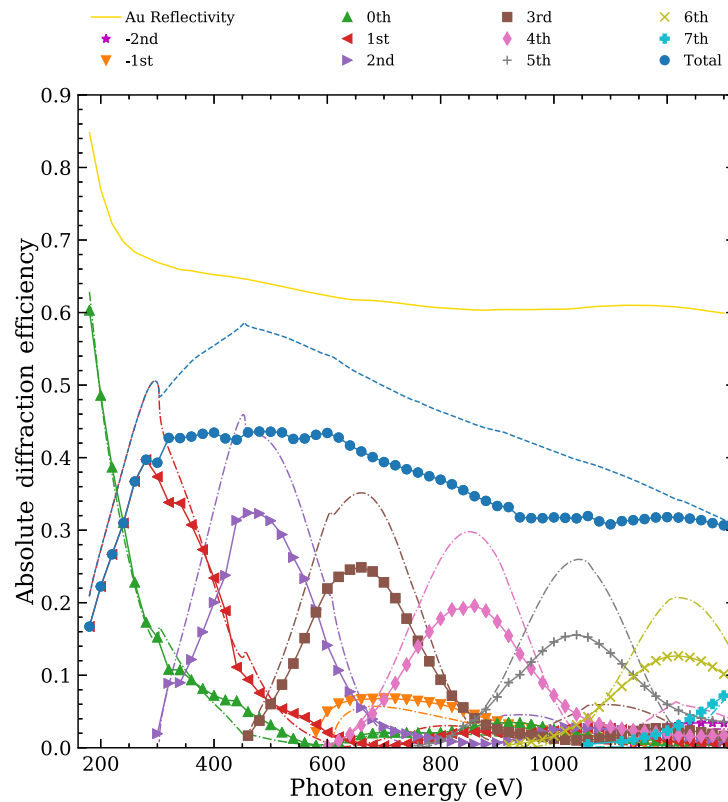


**Fig. 13** Theoretical and measured diffraction efficiency as a function of photon energy. The modeled diffraction efficiency includes the Debye–Waller factor calculated using Eq. (13) with a value of  $\Sigma = 3.5$  nm. The rms surface roughness of the gold layer was set to 0.8 nm. The data are shown as points with connecting lines, while the modeled efficiency from PCGrate is shown as dot-dash lines for the diffraction orders with each modeled order being centered above the corresponding measured order data. The total model efficiency excluding zeroth order is shown as a dashed line. The Au reflectivity for a 0.8-nm rms surface roughness is shown as a solid gold line.

gratings is a result of the smaller grooves necessary to accommodate a 160-nm period. The grayscale profile used to fabricate the 160-nm grating, shown in Fig. 2(a), has two 40-nm-wide steps and one 80-nm-wide step. The profile in the 400-nm TASTE grating used four 100-nm-wide steps. Decreasing the step width increases the sensitivity of the final grayscale profile to electron-scattering effects present during ebeam exposure, which are collectively known as the proximity effect, to the characteristics of the electron beam, and to effects due to the resist. The proximity effect is the result of electrons being injected into the resist at one location and scattering off the resist or the underlying substrate into a different region.<sup>11</sup> These processes act to spread out the electron dose and decrease the lateral dose contrast in adjacent regions, especially smaller ones. While BEAMER adjusts the dose to account for the proximity effect, it is very complicated to model and is imperfect. This has a troublesome effect on small-period grayscale profiles.

An important aspect of TASTE, as the name suggests, is selective topography equilibration, which is a result of regions in a grayscale profile having different molecular weights. These regions will begin to flow at a higher or lower temperature for a larger or smaller molecular weight, respectively.<sup>20</sup> The 160-nm grayscale profile has lower lateral dose contrast between its three smaller regions compared to the lateral dose contrast between the four regions in the 400-nm profile as a result of the proximity effect, the electron beam characteristics, and resist effects making up a larger fraction of the region size. This reduces the lateral molecular-weight contrast, allowing the regions to thermally reflow at similar temperatures. Reflowing the grayscale profile into a blazed profile under these conditions is difficult and limited in what temperatures and reflow times are accessible. The 400-nm grating was reflowed at 116°C for 30 min,<sup>6,7</sup>

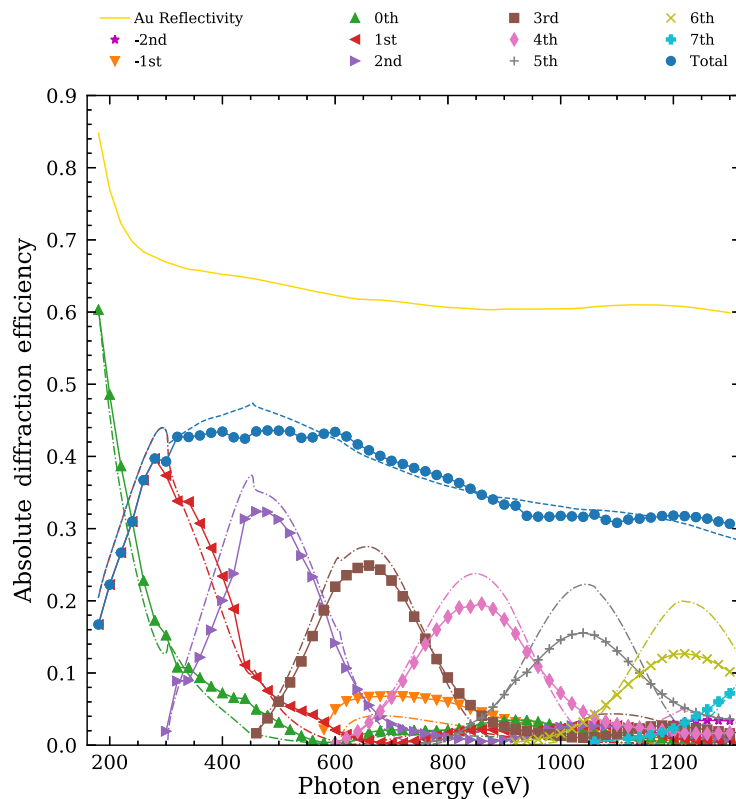


**Fig. 14** Theoretical and measured diffraction efficiency as a function of photon energy. The modeled diffraction efficiency includes the Debye–Waller factor calculated using Eq. (13) with a value of  $\Sigma = 2.35$  nm. The rms surface roughness of the gold layer was set to 2.8 nm. The data are shown as points with connecting lines, while the modeled efficiency from PCGrate is shown as dot-dash lines for the diffraction orders with each modeled order being centered above the corresponding measured order data. The total model efficiency excluding zeroth order is shown as a dashed line. The Au reflectivity for 0.8-nm rms surface roughness is shown as a solid gold line.

whereas the 160-nm period grating was reflowed at 108°C for 15 min. Increasing the reflow time or temperature to allow the profile to better equilibrate led to additional rounding in the profile, while decreasing the temperature could prevent effective reflow altogether. We hypothesize that the decreased selective topography equilibration during the thermal reflow step, resulting from the decreased lateral molecular-weight contrast in the 160-nm period grating, is affecting the roughness profile and causing the difference in performance as compared to the 400-nm TASTE grating. Future work will include measuring the effect of the thermal reflow, lithographic, and deposition processes on the grating roughness profile.

## 5 Conclusion

We have measured the diffraction efficiency of the first x-ray reflection grating fabricated using TASTE with a period of 160 nm. The diffraction efficiency was measured from 180 to 1300 eV using beamline 6.3.2 at Lawrence Berkeley National Laboratory’s ALS. The grating exhibited modest diffraction efficiency with a maximum total efficiency above 40% and single-order efficiency ranging from 10% to 40%. The performance of the grating was lower than gratings previously tested at ALS, such as a 400-nm TASTE grating<sup>7</sup> and a 160-nm replicated KOH grating.<sup>8</sup> The single-order and total diffraction efficiency was lower relative to these gratings as a result of the groove and roughness profiles of the grating. The efficiency loss, which can be clearly seen in the decrease in the relative diffraction efficiency including zeroth order, combined with modeling the efficiency losses due to roughness using the Nevot–Croce and Debye–Waller factors,

suggests that there is a significant amount of diffuse vacuum scattering occurring as a result of the roughness profile of the grating; this is likely due to the correlation length of the roughness features. We hypothesize that the decrease in grating performance compared to the 400-nm TASTE grating is due to nonoptimal selective topography equilibration resulting from the decreased feature sizes necessary to accommodate a 160-nm period.

The measurement results are encouraging for the first attempt at fabricating a TASTE grating with smaller feature sizes. However, additional development is ongoing to increase the performance of TASTE gratings to meet the requirements of Lynx and other future observatories. These efforts include creating sharper blaze facets to increase single-order diffraction efficiency as well as characterizing and improving the roughness profile to reduce scatter and increase total diffraction efficiency. Future gratings tested at beamline 6.3.2 will include measurements to locate and quantify scatter as a function of photon energy in order to better understand its dependence on the grating roughness profile. There is a large amount of fabrication parameter space for TASTE that can be explored to achieve these goals. Example parameters include: ebeam resists, resist thicknesses, developers, developer concentrations, develop times, grayscale patterns, and reflow conditions. TASTE offers a promising path forward for fabricating high-performance, blazed, variable-line-space gratings for future observatories in the x-ray and other wavelengths.

## Acknowledgments

The authors would like to thank Chad Eichfeld and Michael Labella for their assistance with grating fabrication and Eric Gullikson for his support at ALS. This research used resources of the Nanofabrication Laboratory and the Materials Characterization Laboratory at the Materials Research Institute at The Pennsylvania State University, as well as the Advanced Light Source, which is a DOE Office of Science User Facility under contract no. DE-AC02-05CH11231. This work is supported by NASA under Grants Nos. 80NSSC18K0282, NNX17AD19G, and NASA Space Technology Research Fellowships. The authors have no relevant financial interests in the manuscript and no other potential conflicts of interest to disclose.

## References

1. J. A. Gaskin et al., “Lynx X-ray observatory: an overview,” *J. Astron. Telesc. Instrum. Syst.* **5**(2), 021001 (2019).
2. National Research Council, *New Worlds, New Horizons in Astronomy and Astrophysics*, The National Academies Press, Washington, DC (2010).
3. Lynx Collaboration, “Lynx X-ray observatory concept study report,” [www.lynxobservatory.com](http://www.lynxobservatory.com) (2019).
4. R. L. McEntaffer, “Reflection grating concept for the Lynx X-ray grating spectrograph,” *J. Astron. Telesc. Instrum. Syst.* **5**(2), 021002 (2019).
5. W. Cash, “Echelle spectrographs at grazing incidence,” *Appl. Opt.* **21**(4), 710–717 (1982).
6. J. A. McCoy, R. L. McEntaffer, and C. M. Eichfeld, “Fabrication of astronomical x-ray reflection gratings using thermally activated selective topography equilibration,” *J. Vac. Sci. Technol. B* **36**(6) (2018).
7. J. A. McCoy, R. L. McEntaffer, and D. M. Miles, “Extreme ultraviolet and soft x-ray diffraction efficiency of a blazed reflection grating fabricated by thermally activated selective topography equilibration,” *Astrophys. J.* **891**, 114 (2020).
8. D. M. Miles et al., “Fabrication and diffraction efficiency of a large-format, replicated X-ray reflection grating,” *Astrophys. J.* **869**(2), 95 (2018).
9. R. McEntaffer et al., “First results from a next-generation off-plane X-ray diffraction grating,” *Exp. Astron.* **36**(1–2), 389–405 (2013).
10. W. C. Cash, “X-ray spectrographs using radial groove gratings,” *Appl. Opt.* **22**, 3971 (1983).
11. N. Pala and M. Karabiyik, *Electron Beam Lithography (EBL)*, Encyclopedia of Nanotechnology, pp. 1033–1057, Springer Netherlands (2016).

12. A. E. Franke et al., "Super-smooth x-ray reflection grating fabrication," *J. Vac. Sci. Technol. B* **15**(6), 2940–2945 (1997).
13. C. Chang et al., "Fabrication of sawtooth diffraction gratings using nanoimprint lithography," *J. Vac. Sci. Technol. B* **21**(6), 2755–2759 (2003).
14. C. T. DeRoo et al., "Line spread functions of blazed off-plane gratings operated in the Littrow mounting," *J. Astron. Telesc. Instrum. Syst.* **2**(2), 025001 (2016).
15. L. F. Johnson, "Evolution of grating profiles under ion-beam erosion," *Appl. Opt.* **18**, 2559–2574 (1979).
16. Q. Liu, J. Wu, and M. Chen, "Fabrication of blazed grating by native substrate grating mask," *Opt. Eng.* **52**(9), 091706 (2013).
17. A. Schleunitz and H. Schiff, "Fabrication of 3D nanoimprint stamps with continuous reliefs using dose-modulated electron beam lithography and thermal reflow," *J. Micromech. Microeng.* **20**(9), 095002 (2010).
18. A. Schleunitz et al., "Selective profile transformation of electron-beam exposed multilevel resist structures based on a molecular weight dependent thermal reflow," *J. Vac. Sci. Technol. B* **29**(6), 06F302 (2011).
19. A. Schleunitz et al., "Novel 3D micro- and nanofabrication method using thermally activated selective topography equilibration (TASTE) of polymers," *Nano Converg.* **1**(1), 7 (2014).
20. R. Kirchner and H. Schiff, "Thermal reflow of polymers for innovative and smart 3D structures: a review," *Mater. Sci. Semicond. Process.* **92**, 58–72 (2019).
21. R. C. McCurdy et al., "Fabrication and diffraction efficiency of a 160-nm period x-ray reflection grating produced using thermally activated selective topography equilibration," *Proc. SPIE* **11119**, 111190Y (2019).
22. GenISys, "Electron- and laser-beam lithography software," <https://www.genisys-gmbh.com/beamer.html>.
23. E. M. Gullikson, S. Mrowka, and B. B. Kaufmann, "Recent developments in EUV reflectometry at the Advanced Light Source," *Proc. SPIE* **4343**, 363–373 (2001).
24. B. L. Henke, E. M. Gullikson, and J. C. Davis, "X-ray interactions: photoabsorption, scattering, transmission, and reflection at  $E = 50\text{--}30000$  eV,  $Z = 1\text{--}92$ ," *Atomic Data and Nuclear Data Tables* **54**(2), 181–342 (1993).
25. L. Nevot and P. Croce, "Characterization of surfaces by grazing X-ray reflection: Application to the study of the polishing of various silicate glasses," *Rev. Phys. Appl.* **15**, 761–779 (1980).
26. D. K. G. de Boer, "X-ray reflection and transmission by rough surfaces," *Phys. Rev. B* **51**(8), 5297–5305 (1995).
27. D. Attwood and A. Sakdinawat, *X-Rays and Extreme Ultraviolet Radiation: Principles and Applications*, 2nd ed., Cambridge University Press (2017).
28. H. Marlowe et al., "Modeling and empirical characterization of the polarization response of off-plane reflection gratings," *Appl. Opt.* **55**, 5548–5553 (2016).
29. L. I. Goray and G. Schmidt, "Solving conical diffraction grating problems with integral equations," *J. Opt. Soc. Am. A* **27**, 585–597 (2010).
30. A. Kato and F. Scholze, "Effect of line roughness on the diffraction intensities in angular resolved scatterometry," *Appl. Opt.* **49**, 6102 (2010).
31. A. F. Herrero et al., "Applicability of the Debye–Waller damping factor for the determination of the line-edge roughness of lamellar gratings," *Opt. Express* **27**, 32490 (2019).
32. P. Debye, "Interferenz von Röntgenstrahlen und Wärmebewegung," *Ann. Phys.* **348**(1), 49–92 (1913).
33. I. Waller, "Zur Frage der Einwirkung der Wärmebewegung auf die Interferenz von Röntgenstrahlen," *Zeitschr. Phys.* **17**, 398–408 (1923).

**Ross C. McCurdy** is a PhD student at the Pennsylvania State University. He received his BS degrees in physics and astronomy from the University of Iowa in 2017. He is currently working on the fabrication and testing of X-ray reflection gratings for future space-based missions and suborbital rockets.

**Drew M. Miles** is a PhD student at the Pennsylvania State University. He received his BS degree in physics and astronomy from the University of Iowa in 2015. In addition to his work in reflection grating fabrication and testing, he is interested in designing, building, and launching space-based astronomical instruments. He is a member of SPIE.

Biographies of the other authors are not available.